J. Condensed Matter Nucl. Sci. 41 (2026) 170–181

Research Article

Excess Heat and Influences of Temperature and Atmosphere on the Microstructure of Pd-Ni-Zr Alloy Nanopowders

Yanxia Liang, Hui Zhao, Linghui Hou, Dahai Liu, Xinhua Ma,
Junli Hou, Wuyun Xiao*
State Key Laboratory of Chemistry for NBC Hazards Protection, Beijing 102205, China

Wu-Shou Zhang*
Institute of Chemistry, CAS, Beijing 100190, China

Abstract

The Pd-Ni-Zr alloy has been identified as one of the most promising materials for low-energy nuclear reactions (LENR). The simple and efficient fabrication of the Pd-Ni-Zr alloy, in conjunction with systematic investigations into its control factors, significantly advances the progress of LENR. In this study, Pd-Ni-Zr alloy nanopowders with different compositions were prepared by high-energy ball milling and subjected to heat treatment including high-temperature vacuum annealing, high-temperature oxidation and deuterium reduction. The grain refinement process of Pd-Ni-Zr alloy nanopowder was explored based on different ball milling times. The deuterium reduction of Pd-Ni-Zr samples prepared under different ball-milling conditions reached a minimum of 27 nm, accompanied by a high density of defects including dislocations, interfaces, and amorphous structure. From the results of scanning electron microscopy (SEM), transmission electron microscopy (TEM) and X-ray diffraction (XRD), the influence of temperature and atmosphere on the morphology, phase structure, and crystallinity of Pd-Ni-Zr alloy was revealed. Excess heat of Pd-Ni-Zr alloy nanopowder in D_2 was assessed with a high-precision Seebeck calorimeter. Results demonstrate that both the activation treatment (involving high-temperature oxidation and deuterium reduction) and the stepwise variation of reaction temperature are critical factors for enhancing the excess heat of Pd-Ni-Zr alloy. Excess power of 0.6 W (or 120 W/kg of the sample) was obtained with the optimized Pd-Ni-Zr alloy samples.
 ISSN 2227-3123

Keywords: High-energy ball milling, Pd-Ni-Zr, Heat treatment, Microstructure, Seebeck calorimetry

1. Introduction

Pd-based alloys have proven to be an effective material for promoting low-energy nuclear reactions (LENR) since Pd-Ni alloys were first reported in the field [1]–[4]. On the other hand, Pd-Ni alloys are widely used in hydrogen

*Corresponding authors: W.-S. Zhang and W. Xiao

© 2026 ICCF. All rights reserved. ISSN 2227-3123

energy applications due to their excellent catalytic ability and cost-effectiveness [5]–[8]. Previous studies revealed that the properties of metallic nanocrystals are significantly influenced by their composition, shape and structure [9]–[11]. It has been demonstrated that a nanograin structure enhances the adsorption performance of materials in interactions with hydrogen [5], [12]–[14]. Given the noble metal attributes and scarcity of Pd, enhancing per-atom efficiency remains a critical goal in current research.

In addition, incorporating non-noble metal elements into Pd-based materials can effectively enhance the activity through the synergistic structural and electronic effects, while also reducing the amount of Pd usage. Significant discoveries have been made in the field of LENR through the use of Pd-Ni-Zr ternary alloys, which are formed by incorporating ZrO_2 into nickel-palladium alloys. A. Kitamura *et al.* fabricated Pd-Ni-Zr ternary alloys by alloy smelting, mechanically pulverized them to micrometer-scale dimensions, and then performed hydrogen/deuterium charging experiments, which produced anomalous excess heat [15]. They further observed that repeated calcination and oxidation processes enhanced the magnitude of the excess heat [3], [16]. Therefore, temperature and atmospheric conditions are crucial for activating materials to produce larger excess heat. However, the influence of heat treatment parameters on the microstructure of materials remains unclear.

Chemical synthesis methods are predominantly employed to produce Pd-based nanomaterials [17]. However, constrained by the limited single-batch synthesis quantity and strict selectivity for chemical elements, chemical synthesis methods are not suitable for LENR. High-energy ball milling (HEBM) is recognized as a versatile mechanical synthesis technique in nanomaterials, widely used in the ultrafine processing of metals, ceramics, and biomaterials [18]–[20]. HEBM enables efficient reduction of raw material particles to the nanoscale under simple and impurity-free conditions, achieved by mechanical collision and friction forces between grinding balls and raw powders [21]. Notably, it also generates nanoscale defects that contribute to enhanced material performance. The nanocrystalline/amorphous structure of Al-Fe-Nb powders is controlled with HEBM, which renders the powders more suitable for applications demanding high thermal stability and customized magnetic response [22], [23]. By regulating milling parameters, precise control over the microstructure of alloy powders can be achieved.

In this paper, Pd-Ni-Zr alloy nanopowder with the average particle size of 27 nm was prepared by HEBM, and subjected to heat treatment including high-temperature vacuum annealing, high-temperature oxidation and deuterium reduction. By characterizing samples at different ball milling stages and those subjected to heat treatment under various conditions, using scanning electron microscopy (SEM), transmission electron microscopy (TEM) and X-ray diffraction (XRD), this study identified the Pd-Ni-Zr grain control factors and the influence of heat treatment parameters on the microstructure. Calorimetry was carried out on the treated samples under deuterium gas charging and discharging conditions, and the results showed that the pretreated samples exhibited clear-cut excess heat of 0.6 W.

2. Experiments

To prepare Pd-Ni-Zr alloy nanopowder, pure Pd, Ni and ZrO_2 powders (all from Alfa Aesar) were used as initial materials. The HEBM was performed using a Fritsch P-7 reinforced planetary ball mill (Fritsch GmbH, Germany). The ball milling process was conducted at room temperature with a rotation speed of 500 rpm. The ratio of the grinding jar rotation to its revolution speed was maintained at 1:2. The ball-to-powder ratio (BPR) of 15:1 was adopted in the experiment using grinding balls of 1 mm diameter. Wet ball milling was utilized to improve ball milling efficiency and reduce material adhesion to the grinding jar wall, where chromatographic grade ethanol (purity > 99.997%, Aladdin Scientific Corp.) was used as the process control agent. SEM equipped with energy dispersive spectroscopy (EDS), TEM and XRD were employed to characterize the microstructure and phase structure of the samples. Nano Measurer software was utilized for particle size statistics, and the Martin diameter (the length of the area bisector of polygonal particles measured horizontally) was used to define the particle diameter.

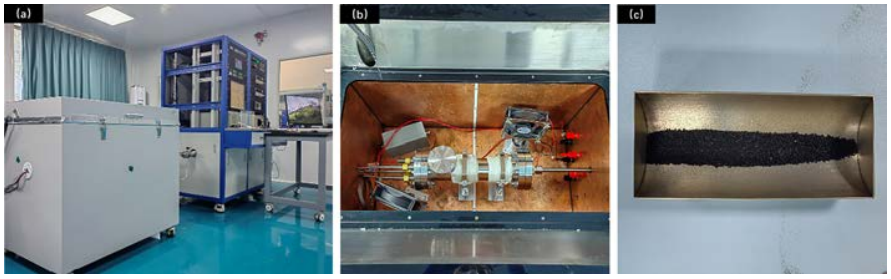

Figure 1. The calorimetric system. (a) Seebeck calorimeter and the control systems, (b) reactor in the calorimeter chamber, and (c) sample boat with Pd-Ni-Zr samples.

The Pd-Ni-Zr alloy nanopowder obtained by HEBM was subjected to vacuum drying. Subsequently, the samples were placed into the atmospheric treatment system (NMS, RCL) for heat treatment in three phases:

- High-temperature vacuum annealing: the vacuum pump was used to evacuate the sample tube until the vacuum level reached better than 10^{-4} Pa. The annealing temperature was 500°C with a heating rate of 7°C/min and a holding time of 600 min.
- High-temperature oxidation: the heating process and temperature holding conditions were the same as those for the high-temperature vacuum annealing. Throughout the heating process, the sample was maintained in a flowing air atmosphere.
- Deuterium reduction: the oxidized samples were placed in the atmospheric treatment system for deuteration. After the vacuum level reached better than 10^{-4} Pa, deuterium gas was filled into the tube until a stable pressure (approximately 20 kPa) was achieved. The heating process and temperature were the same as those for the high-temperature vacuum annealing. After deuterium reduction, the deuterated samples were allowed to cool naturally to room temperature.

The measurement of excess heat for the heat-treated samples was conducted using a high-precision calorimetric system, as shown in Figure 1. The calorimetric system includes a Seebeck calorimeter, temperature and gas circuit control system (Figure 1(a)), as well as a reactor serving as the reaction chamber (Figure 1(b)). Pd-Ni-Zr alloy nanopowder was placed in a sample boat made of pure nickel (Figure 1(c)), which was then placed in the reaction chamber. Tests of excess heat for LENR were performed under controlled conditions of temperature and hydrogen/deuterium gas pressure.

To guarantee the accuracy of the heat measurement, the calorimetric experiments consist of the following steps: sample loading, vacuum pumping, gas flushing, helium-based calibration, blank experiment, and deuterium charging experiment. Prior to the final charging of hydrogen or deuterium gas, it is necessary to ensure the purity of the atmosphere through gas displacement and cyclic purification, which is crucial to avoid the influence of redox heat. During calorimeter calibration, helium gas was introduced into the reactor. Calibration was performed at five power steps, with input power from 0 to 200 W. Each power level step lasted for 480 minutes and only the most stable output signals of 30 minutes were used. In blank experiments, nitrogen gas was introduced into the reactor, followed by the heating program and calorimetric programs described above. In deuterium-charging calorimetry experiments, the reactor must be cyclically refilled with deuterium gas to determine how deuterium cycles affect performance. Calibrations were repeated after deuterium-charging calorimetry to ensure data accuracy and reproducibility, and to reduce drift caused by environmental changes or system program instability.

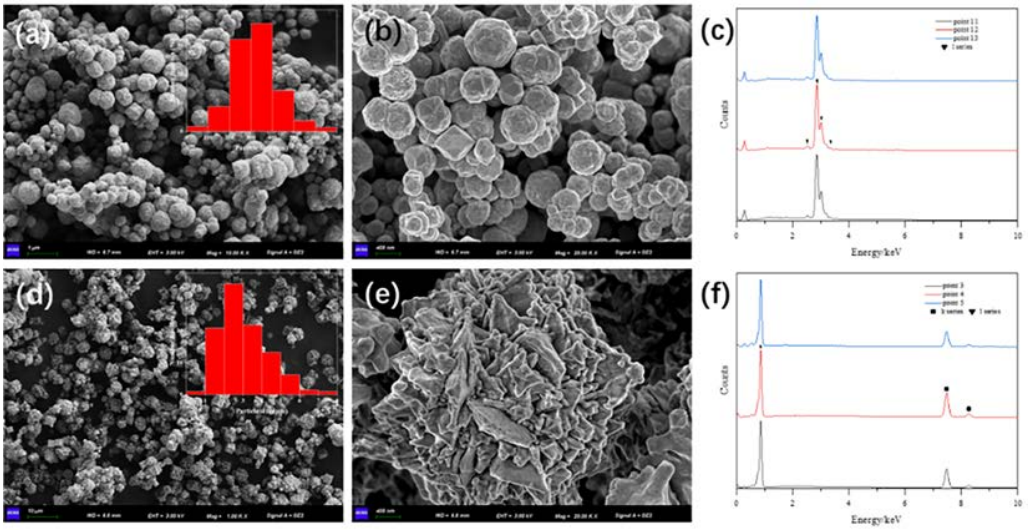

Figure 2. (a) SEM, (b) enlarged image and (c) EDS of initial Pd powder. (d) SEM, (e) enlarged image and (f) EDS of initial Ni powder. Insets are the corresponding statistical histograms.

3. Results and Discussion

3.1. The Microstructure of Pd-Ni-Zr Alloy Nanopowder Obtained With HEBM

Before synthesizing the Pd-Ni-Zr alloy nanopowder with ball milling, the microstructural and composition of the original materials were characterized. Figure 2 shows SEM images of the original Pd and Ni powder at different magnifications, as well as the size distribution and element spectra. The original Pd powder shown in Figures 2(a) and 2(b) has a nearly spherical structure, and the surface has a rough and undulating texture. While a number of small particles exhibit aggregation, individual particles remain distinguishable, with all particles in the aggregates included in the histogram analysis. The average Pd particle size is about 320 nm from the histogram in the inset in Figure 2(a). Figure 2(c) presents the EDS at three points in different regions of Pd powder, with all peak positions corresponding to the element Pd. The original Ni powder shown in Figure 2(d) has an approximately polygonal shape, and the magnified SEM image presented in Figure 2(e) shows that its surface structure exhibits a sawtooth structure. The statistical histogram in the inset of Figure 2(d) reveals an average particle diameter of 3.1 μm for the Ni powder. The EDS result shown in Figure 2(f) confirms that the composition of this powder is pure Ni. The sample information of the initial ZrO_2 is consistent with that in the previous work [24], and thus no further elaboration is given herein.

Samples with atomic ratios of Pd:Ni:Zr = 1:7:1 (labeled as PNZ_1) and Pd:Ni:Zr = 1:7:7 (labeled as PNZ_7) were prepared with HEBM. Figure 3 presents the SEM images of PNZ_1 at various ball milling stages, along with the diagram of particle size variation with ball milling time. During the early stage of ball milling (Figure 3(a)), the particles exhibit an irregular morphology. The particle size is relatively large, while the distribution of particles is highly inhomogeneous. The surfaces of larger particles are coated with tiny particles. This can be attributed to the fact that Pd and Ni experience plastic deformation under the action of impact forces along the axial direction, leading to a reduction in the axial size while stretched in the radial direction. Meanwhile, ZrO_2 is rapidly crushed into nano-sized particles under the action of forces, which then coat the surfaces of large particles. With the increase of ball milling time, the relatively thin regions on the particle edges break off due to impact forces and friction, leading to an

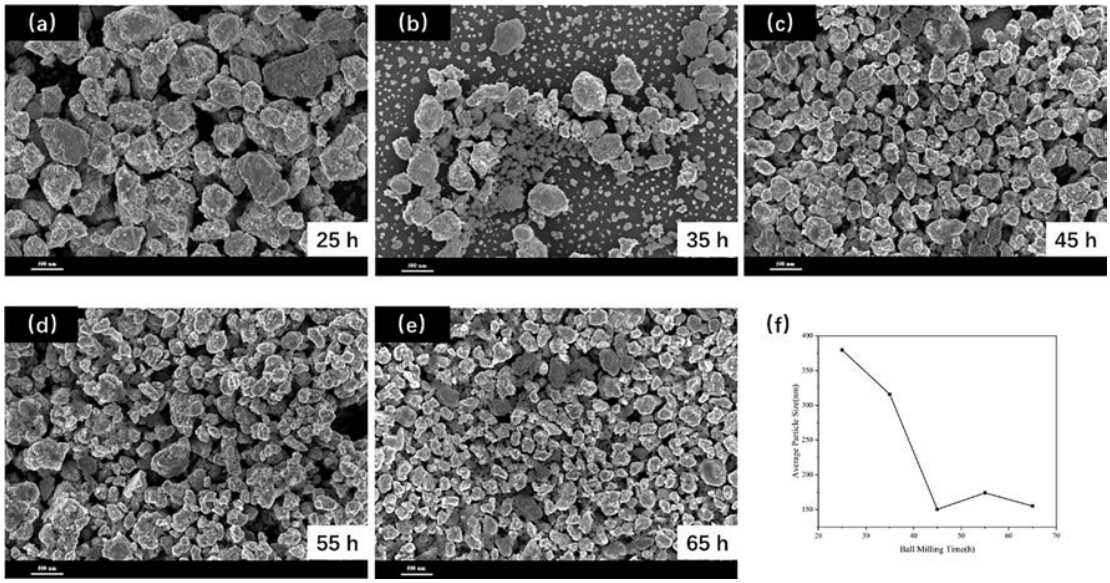

Figure 3. SEM images of PNZ_1 (i.e. $PdNi_7(ZrO_2)$) powder ball milled for (a) 25 h, (b) 35 h, (c) 45 h, (d) 55 h, and (e) 65 h and (f) the relationship between the average size of PNZ_1 particle and ball milling time.

increase in the density of small-diameter particles (Figure 3(b)). Pd, Ni and ZrO_2 powders further integrate with the continuous progress of ball milling. Due to the pinning effect exerted by ZrO_2, the average particle diameter of the entire alloy nanopowder decreases rapidly. As ball milling time further increases to 45 h, the particle size of PNZ_1 powder decreases to less than 200 nm (Figure 3(c)). The ball milling process ultimately reaches a state of dynamic balance as particle fragmentation and agglomeration rates become nearly equal. In this stage, the particle size of the sample varies with time without obvious reduction (Figure 3(d) and 3(e)), and its average particle diameter is about 149 nm. Figure 3(f) shows the relationship between the average size of PNZ_1 particle and ball milling time, presenting the time of the powder particles in different ball milling stages as well as the particle size corresponding to each stage.

The particle fragmentation process of PNZ_7 sample is similar to that of PNZ_1. In terms of the final equilibrium particle size, the average particle size of PNZ_7 sample is about 27 nm with the maximum particle diameter of 119 nm, and the minimum diameter of 11 nm, which is smaller than that of PNZ_1. The PNZ_7 sample exhibits a significantly enhanced refinement effect on the alloy powder due to the increased atomic ratio of ZrO_2 powder.

To clarify the crystalline microstructure and defects of the alloy nanopowder, TEM characterization was performed on the PNZ_7 sample, as shown in Figure 4. TEM bright-field image (Figure 4(a)) of typical PNZ_7 particles indicates that this material consists entirely of nanocrystals with rough boundaries. The polycrystalline ring illustrated in the selected area electron diffraction (SAED) pattern (top-right inset in Figure 4(a)) indicates that the polycrystalline with small grain size has more complex crystal orientations. The statistical result of grain size in this region (bottom-right inset in Figure 4(a)) indicates that the largest grain size is 42 nm and the smallest is 5 nm, and the average grain size is 16 nm. Figure 4(b) is a high-resolution TEM image of one PNZ_7 grain with a size of about 25 nm, and the fast Fourier transform (FFT) patterns (bottom-right inset in Figure 4(b)) show the diffraction points clearly.

Figures 4(c) and 4(d) represent the interfacial and internal microstructure of PNZ_7 nanoparticles. The rough grain boundary (marked by yellow dotted curve) shown in Figure 4(d) indicates that abundant interfacial atoms exist

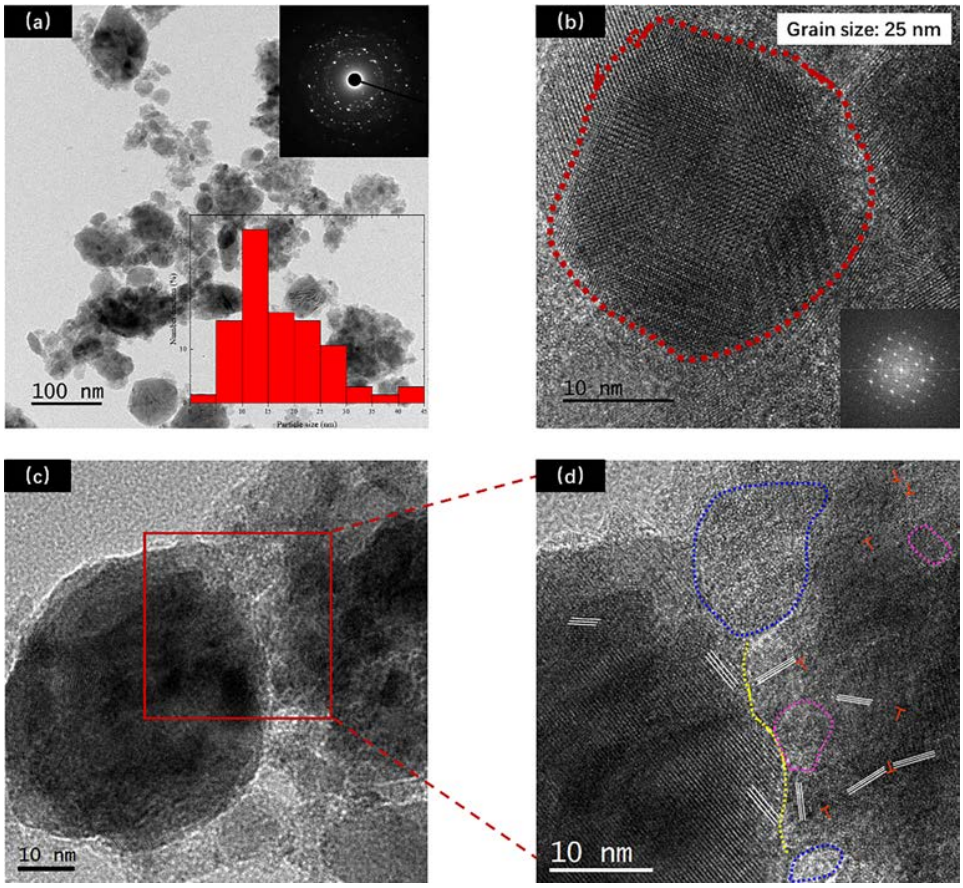

Figure 4. TEM of PNZ_7 (i.e. $PdNi_7(ZrO_2)_7$) sample. (a) TEM bright-field image. The top-right inset is SAED pattern and bottom-right inset is a grain size statistical histogram. (b) High-resolution TEM of the grain with FFT pattern. (c) Low-magnification image and (d) high-magnification image of interfacial and internal microstructure. The grain boundary is marked by yellow dotted lines, the amorphous regions between grains are marked by blue dotted curves and the intragranular amorphous regions are marked by pink dotted curves. White parallel lines represent different crystal orientations and the red T-shaped marks represent dislocation defects.

in the ball-milled powders. In addition, the sample also contains amorphous regions, which can be divided into interfacial amorphous regions (marked by blue dotted curves) and intragranular amorphous regions (marked by pink dotted curves). By comparing the two kinds of amorphous structures, it is found that the area of amorphous regions at the crystal edges is larger than that of amorphous regions inside the crystals. This finding is related to the amorphous formation energy. Due to the higher atomic surface energy at the crystal boundaries, amorphous phases form more easily in these areas. In contrast, atoms inside the crystals have a stronger tendency to arrange into an ordered structure, which not only makes amorphous formation more difficult but also hinders the expansion of existing amorphous regions. Numerous crystal orientations (marked by white parallel lines) and dislocations (marked by red “T” marks) also exist inside the PNZ_7 nanocrystals. Atoms at the interfaces and dislocations are in an asymmetric high-energy

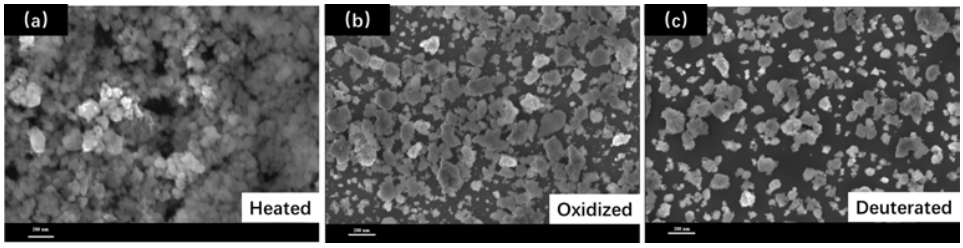

Figure 5. SEM images of PNZ_7 powder samples after (a) high-temperature vacuum annealing, (b) high-temperature oxidation, and (c) high-temperature deuterium reduction.

state, which in turn exerts an effect on the interaction between hydrogen and deuterium. This is considered one of the key factors influencing the LENR performance of PNZ alloys.

3.2. Effects of Temperature and Atmosphere on Microstructure of Pd-Ni-Zr Alloy Nanopowder

Previous studies have shown that repeated calcination of Pd-Ni-Zr alloy in air can enhance the anomalous exothermic performance under hydrogen/deuterium atmosphere [15], [16]. To clarify the influence of heat treatment conditions on the microstructure of Pd-Ni-Zr alloy nanopowder, material activation methods including high-temperature vacuum annealing, high-temperature oxidation and deuterium reduction were applied to PNZ_7. Figure 5 presents SEM of the PNZ_7 samples after different heat treatment conditions. The particle morphology (see Figure 5(a)) of the sample treated by high-temperature vacuum annealing shows almost no change compared with the original powder. However, the agglomeration phenomenon becomes more severe with the particle size increasing to 45 nm. Small particles dissolve and are absorbed by larger particles at high temperatures, thereby promoting continuous growth. Figure 5(b) shows the SEM of PNZ_7 powder treated by high-temperature oxidation, which reveals oxidative sintering between particles and a consequent increase in the size of some particles. Additionally, the particle sizes exhibit partial non-uniformity, with unsintered small particles adhering to the surfaces of large particles. Compared with the sample after ball milling, the average particle size of the oxidation-treated sample rises significantly to 147 nm. Figure 5(c) presents the SEM image of the PNZ_7 powder sample after high-temperature deuterium reduction treatment. After deuterium reduction, the density of small-sized particles in the sample is higher than that in the oxidized sample. This is probably the result of hydrogen embrittlement. Meanwhile, small-sized particles generally exhibit a morphology where they agglomerate tightly to form a single large particle. Compared to the large-particle powder formed after oxidative sintering, the deuterated sample exhibits a higher specific surface area.

The particle size affects adsorption performance primarily because it directly modifies the effective interaction conditions between metal and hydrogen/deuterium. Specifically, smaller particles typically increase the specific surface area to provide more adsorption sites, reduce diffusion resistance by accelerating the transport of hydrogen/deuterium to the active sites of the material, and enhance mass transfer efficiency. However, particle agglomeration can block the adsorption pores and impair the adsorption process.

Particle size affects the hydrogen/deuterium adsorption performance of alloy powders significantly, and the phase composition of alloy powder is also a factor influencing the interaction between the material and hydrogen/deuterium. Herein, XRD tests were performed to reveal the effect of heat treatment on the phase composition of Pd-Ni-Zr alloy nanopowder, as shown in Figure 6. The gray pattern in Figure 6 corresponds to the constituent phases of the ball-milled PNZ_7 powder sample, indicating that the as-prepared sample mainly consists of the PdNiZr, NiZr and PdZr compound phases. In addition, a portion of the ZrO_2 phase was retained after the ball milling due to the relatively high addition amount of ZrO_2 in the PNZ_7 sample. The broadening of peaks indicates small crystallite size according

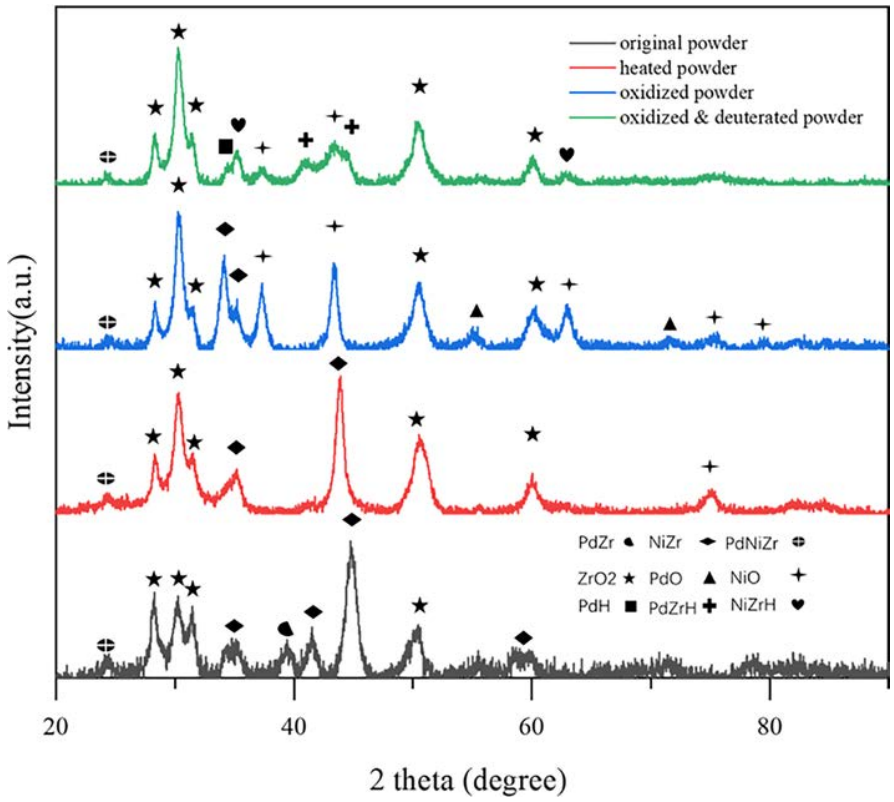

Figure 6. XRD patterns of original PNZ_7 powder sample (the gray spectrum), the sample after high-temperature vacuum annealing (the red spectrum), the sample after high-temperature oxidation (the blue spectrum), and the sample after high-temperature deuterium reduction (the green spectrum).

to the Scherrer equation. After the prepared PNZ_7 sample was subjected to high-temperature vacuum annealing, the full width at half maximum (FWHM) of diffraction peaks narrowed, which corresponds to the increase of grain size. Meanwhile, new phase constituents including a small amount of NiO were generated as shown in the red spectrum in Figure 6. The blue and green patterns in Figure 6 correspond to the phases of the PNZ_7 sample after high-temperature oxidation and deuterium reduction respectively. The FWHM of diffraction peaks become narrower for the samples subjected to oxidation and deuterium reduction. It suggests that the grain size increases further, which is consistent with the SEM results in Figure 5. Besides, more oxide components (such as PdO and NiO) appear in the oxidized sample, and hydride components (such as PdH, PdZrH and NiZrH) are present in the deuterated sample.

High-temperature treatment applied to the sample enhances the kinetic energy of the particles, which promotes their combination and the formation of particles with a larger size. Although the standard Gibbs free energy of formation indicates that Zr has a stronger binding capacity to oxygen than Ni, a small amount of free oxygen in ball-milled PNZ_7 is captured by Ni in the process of element enrichment at high temperature. Consequently, a minor amount of NiO phase forms in the sample after the high-temperature vacuum treatment. Under oxygen-sufficient conditions, elements such as Pd and Zr will combine with oxygen to form oxides. Consequently, the NiZr alloy phase disappears while the

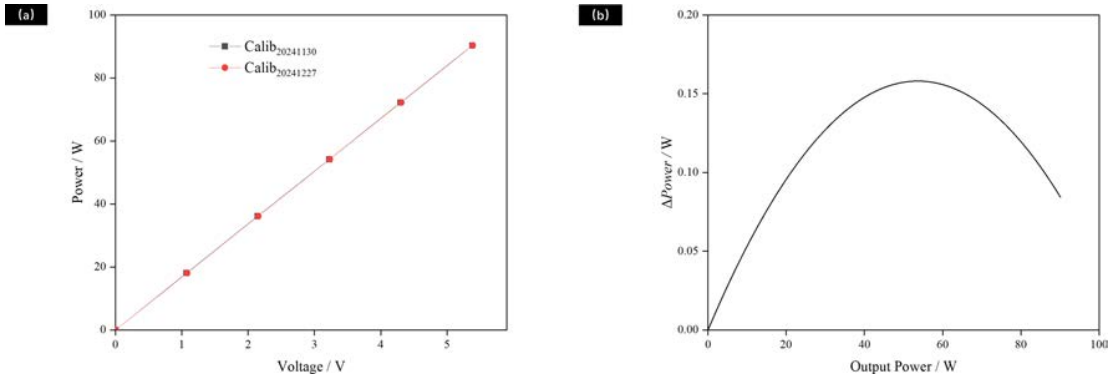

Figure 7. (a) The relationship between the output signal of Seebeck calorimeter and input thermal power. (b) Comparison of the difference between two calibrations before and after the test.

phases of PdO, NiO, and ZrO_2 increase. In contrast, some oxide phase components are reduced by deuterium to form hydrides under high-temperature deuterium conditions.

3.3. Excess Heat of Pd-Ni-Zr Alloy Nanopowders

The LENR experiment, which involves charging hydrogen/deuterium into metal samples and performing calorimetry after heating, is characterized by a long experimental cycle and stringent requirements for control of the experimental conditions. To improve accuracy, the Seebeck calorimeter was calibrated just before and after the test. Figure 7(a) shows the relationship, which can be fitted with a quadratic form, between the output signal of Seebeck calorimeter and the corresponding input power during the two calibrations (marked by $\mathrm{Calib}_{20241130}$ and $\mathrm{Calib}_{20241227}$). Figure 7(b) presents the difference between $\mathrm{Calib}_{20241130}$ and $\mathrm{Calib}_{20241227}$ under the same input power. The discrepancy reaches the maximum of 158 mW with the input power of 53 W, and 82 mW with the thermal power of 90 W. This means the calorimetric error was less than 0.16 W up to 90 W during the period from Nov. 30 to Dec. 27, 2024.

The excess heat from activated samples is more pronounced than from untreated PNZ_7 samples. Figure 8(a) shows the changes in heating current, input power, excess power, temperature and pressure over time in a deuterium-charging 5 g sample of PNZ_7 alloy nanopowders. It is evident that the temperature increases four times caused by a gradual increase of power, and each increase in power was accompanied by a change in both current and voltage (black curve in Figure 8(a)). To simplify interpreting the data, the excess power after each current adjustment must be monitored for more than 6 hours (the relaxation time of the calorimeter). The calorimeter maintains a constant external temperature of $25 \pm 0.01^{\circ}\mathrm{C}$ in a water bath to ensure the accuracy of calorimetry (green curve in Figure 8(a)). The topmost graph in Figure 8(a) demonstrates that an increase in input power leads to a rise in the sample temperature and an increase in the pressure inside the reactor.

A blank experiment began with the charging of N_2 into the reactor. No excess power was detected during this process. In contrast, when D_2 was introduced during the target experiments, excess power was generated to varying extents. Figures 8(b) and 8(c) respectively show the variations of excess power (indicated by the blue curves), input power (indicated by the black curves), and temperature (indicated by the red curves) over time during the two deuterium experiments. Overall, the initial input power in Figure 8(b) is 85 W, the same as the final input power in Figure 8(c), while the initial power in Figure 8(c) is 65 W, the same as the final power in Figure 8(b). By comparing the excess power results of the two experiments, it is found that regardless of whether the initial input power is 65 W or 85 W, neither test produces excess power at the very beginning. However, the temperature change caused by the variation of

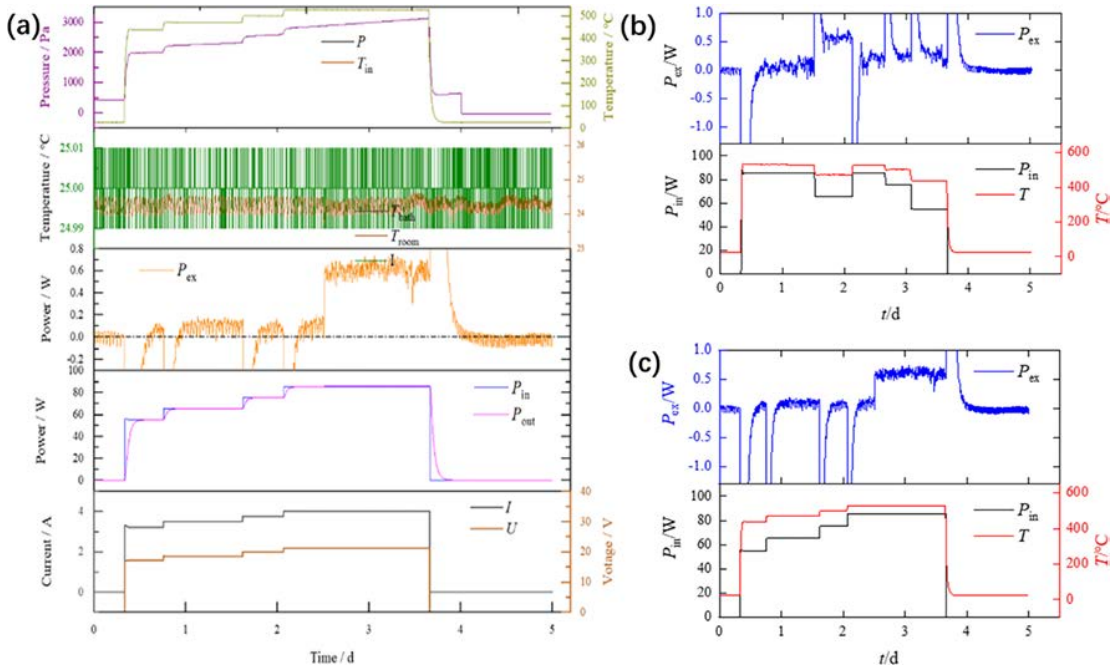

Figure 8. (a) The changes in heating current, input power, excess power, temperature, and pressure in the calorimetric system over time. During the (b) temperature-rise and (c) temperature-fall process, the changes in excess power (blue curves), input power (black curves), and temperature (red curves) over time.

input power disrupts the adsorption equilibrium of the materials within the reactor, resulting in continuous changes in the adsorption and desorption of deuterium within the materials, and leading to the emergence of excess power. When the input power decreases from 85 W to 65 W, the temperature drops from 530°C to 473°C, and the excess power increases from 51 ± 93 mW to 564 ± 82 mW, showing excess power significantly higher than the standard deviation. When input power is restored to the higher level, the temperature rises to 527°C. The excess power decreases but still exists, with a value of 232 ± 94 mW, which is greater than twice the standard deviation. In the experiment shown in Figure 8(c), the initial input power is 65 W, the temperature is 470°C, and the excess power is 105 ± 82 mW, which indicates no statistically significant excess power. As the power increases to 85 W and the temperature rises to 526°C, the excess power also increases to 613 ± 94 mW.

4. Conclusions

Pd-Ni-Zr alloy nanopowder with different atomic ratios was successfully prepared by high-energy ball milling. The microstructure of the samples was analyzed in detail to clarify the particle refinement process and the microstructural features of the Pd-Ni-Zr alloy nanopowder. The powders with atomic ratios of Pd:Ni:Zr = 1:7:1 and Pd:Ni:Zr = 1:7:7 achieved average particle sizes of 149 nm and 27 nm, respectively. A large number of interface structures, amorphous regions, and defects are present inside the Pd-Ni-Zr alloy nanopowder, which are believed to promote the interaction between metal atoms and hydrogen/deuterium. Moreover, the high-temperature and atmosphere treatment of the samples leads to an increase in the particle size of the Pd-Ni-Zr powders as well as changes in their morphol-

ogy and phase composition, thereby influencing the hydrogen/deuterium adsorption-desorption processes. A more scientific and reliable calorimetric experimental method was proposed in this paper. Through deuterium charging calorimetry tests conducted on the alloy nanopowder, the significance of temperature changes in the production of excess power was identified, and excess power of 613 $\pm$ 94 mW was obtained with 5 g of treated Pd-Ni-Zr powder.

Acknowledgements

Y. X. Liang and H. Zhao contributed equally. This work was supported by NSFC (12205371, 21153003 and 22373106) and State Key Laboratory of Chemistry for NBC Hazards Protection.

References

[1] P. Mosier-Boss, S. Szpak, F. Gordon, L. Forsley, Use of CR-39 in Pd/D co-deposition experiments. *Eur. Phys. J. Appl. Phys.* **40** (2007) 293–303.

[2] Y. Miyoshi, H. Sakoh, A. Taniike, A. Kitamura, A. Takahashi, R. Seto, Y. Fujita, Effect of forced oxidation on hydrogen isotope absorption/adsorption characteristics of Pd-Ni-Zr oxide compounds. *J. Condensed Matter Nucl. Sci*. **10** (2013) 46–62.

[3] Y. Iwamura, T. Itoh, J. Kasagi, A. Kitamura, A. Takahashi, et al., Anomalous heat effects induced by metal nano-composites and hydrogen gas. *J. Condensed Matter Nucl. Sci.* **29** (2019) 119–128.

[4] A. Takahashi, T. Yokose, Y. Mori, A. Taniike, Y. Furuyama, H. Ido, A. Hattori, R. Seto, A. Kamei, J. Hachisuka, Latest progress in research on AHE and circumstantial nuclear evidence by interaction of nano-metal and H(D)-gas. *J. Condensed Matter Nucl. Sci.* **33** (2020) 14–32.

[5] M. Thi, T. Tran, P. Anh, H. Nhac, Q. Bui, An innovative catalyst of nickel-palladium alloy nanocrystals embedded nitrogen-doped graphene for efficient oxygen reduction reaction. *J. Alloy. Comp.* **79** (2019) 314–324.

[6] L. Kravchuk and N. Ivashchenko, Palladium nickel zirconium oxide catalyst for low-temperature oxidation of carbon monoxide. *Russ. J. Appl. Chem.* **71** (1998) 645–647.

[7] S. Van Wyk, M. Onani, E. Nordlander, Bimetallic nickel and palladium complexes for catalytic applications. *Chem. Pap.* **70** (2016) 1003–1023.

[8] U. Kamarulzaman, M. Rahman, M. Su, Improvement of the performance of dye-sensitized solar cells employing Nickel-Palladium alloy-reduced graphene oxide counter electrode: influence of palladium content. *Optik.* **276** (2023) 170658.

[9] V. Tuong, S. Dong, D. Thanh, O. Geun, S. Gi-Seung, Y. Yeon-Tae, Alloy core composition effect of Pd-Au-alloy @ZnO core-shell nanoparticles on hydrogen gas sensing performance. *Chem. Eng. J.* **483** (2024) 149050.

[10] P. Filomena, A. Rui, F. Carlos, C. Carlos, G. Ibrahim, Effect of syngas composition on hydrogen permeation through a Pd-Ag membrane. *Fuel*. **103** (2013) 444–453.

[11] P. Mariya, S. Shcherbakova, A. Saraev, A. Knyazev, I. Kurzina, Pd-Bi-based catalysts for selective oxidation of glucose into gluconic acid: the role of local environment of nanoparticles in dependence of their composition. *Catalysts* **14** (2024) 66.

[12] S. Lu, Y. Hu, M. Hao, L. Xiong, D. Ma, Q. Yue, Interlayer-confined synthesis of sub-nanometer high-entropy alloys for high-efficiency oxygen reduction. *Nano Research.* **18** (2025) 94907908.

[13] C. Mei, J. Liu, P. Chuang, T. Song, F. Tang, H. Su, J. Huang, Y. Wu, High-temperature ferromagnetism of Ni-doped $\mathrm{PbPdO_2}$ nanograin films synthesized by sol-gel spin-coating method. *Ceram. Int.* **43** (2017) 1997–2003.

[14] J. Huang, T. Odoom, X. Jing et al., Plant-mediated synthesis of zinc oxide supported nickel-palladium alloy catalyst for the selective hydrogenation of 1,3-butadiene. *ChemCatChem.* **9** (2017) 870–881.

[15] A. Kitamura, A. Takahashi, K. Takahashi, R. Seto, T. Hatano, et al., Excess heat evolution from nanocomposite samples under exposure to hydrogen isotope gases. *Int. J. Hydrogen Energy* **43** (2018) 16187–16200.

[16] T. Kobayashi, J. Shigemura, K. Naitoh, Temperature and pressure dependence of anomalous heat generation occurring in hydrogen gas absorption by metal powder. *J. Condensed Matter Nucl. Sci.* **36** (2022) 318–326.

[17] D. Han, Z. Zhang, Z. Bao, H. Xing, Q. Ren, Pd-Ni nanoparticles supported on titanium oxide as effective catalysts for Suzuki-Miyaura coupling reactions. *Front. Chem. Sci. Eng.* **12** (2018) 24–31.

[18] X. Yu, S. Wu, Z. Zhang, C. Wang, Application of ball milling technology in removal of PFAS and ball milling modified materials: A review. *J. Hazard. Mater. Adv.* **18** (2025) 100709.

[19] T. El-Sayed, A. Aboelnaga, M. El-Atawy, M. Hagar, Ball milling promoted N-heterocycles synthesis. *Molecules* **23** (2018) 1348.
[20] A. Hafs, T. Hafs, D. Berdjane, L. Yandjah, N. Hasnaoui, Investigating on structural, microstructural and magnetic properties of nanocrystalline $Fe_{60}Al_{35}Mg_5$ alloy synthesised by high-energy ball milling. *Trans. Indian. Inst. Met.* **76** (2023) 3447–3454.
[21] Y. Liang, Z. Wu, E. Fu, J. Du, P. Wang, Y. Zhao, Y. Qiu, Z. Hu, Refinement process and mechanisms of tungsten powder by high energy ball milling. *Int. J. Refract. Met. Hard Mater.* **67** (2017) 1–8.
[22] N. Oanh, D. An, N. Viet, Nanocrystalline/amorphous tuning of Al-Fe-Nb (Mn) alloy powders produced via high-energy ball milling. *Materials* **17** (2024) 5627.
[23] M. Akmal, A. Malik, W. Jeong, H. Ryu, Incorporating microstructural and mechanical heterogeneity to Ti-Zr-Nb alloy by partial high-energy ball milling. *Mater. Chem. Phys.* **315** (2024) 129037.
[24] H. Zhao, Y. Liang, W. Xiao, W.-S. Zhang, D. Liu, X. Ma, Refinement process and mechanism of nano Cu-Ni-Zr alloy by high-energy ball milling. *J. Condensed Matter Nucl. Sci.* **39** (2024) 130–139.